

Microseisms: Coastal and Pelagic Sources¹

RICHARD A. HAUBRICH

*Institute of Geophysics and Planetary Physics
University of California, La Jolla, California 92037*

KEITH McCAMY

Lamont Geological Observatory, Columbia University, New York 10964

Abstract. Wave-number frequency spectra of seismic background recordings from the large aperture seismic array (LASA) in eastern Montana have been used to study the source locations of different wave types in the frequency band from 40 to 500 mHz. Microseisms in this band consist of surface waves of the Rayleigh and Love type and compressional body waves. The peak power band near 140 mHz (7-sec microseisms) and the lower frequency band near 70 mHz consist of fundamental Rayleigh waves, which often come from the same direction. This is especially true for directions from coasts in the vicinity of large storms. The average directional properties of the two bands are similar, indicating coastal sources for both. Love waves and higher mode Rayleigh waves in some instances come from the same coastal directions as the fundamental mode. Compressional body wave sources, pinpointed by using horizontal phase velocity to measure range, occur near storms both in coastal and pelagic regions. Pelagic storm sources were found only at frequencies that were high compared with double the frequency of ocean waves having a group velocity equal to the storm velocity. Located in the wake of a moving storm, such sources appear to be due to the oppositely traveling waves set up when a storm moves faster than its waves.

1. INTRODUCTION

The low-level background unrest of the earth, called microseisms or earth noise, has puzzled seismologists and other scientists for nearly a century. The problem of its nature and causes has proved particularly unyielding, not, however, for lack of investigation. A bibliography covering work up to 1955 [*Gutenberg and Andrews, 1956*] lists over 600 articles on the subject; one covering the years from 1955 to 1964 [*Hjortenberg, 1967*] lists 566. Unfortunately, much of this work has advanced the subject but slightly. In a recent review *Iyer* [1964] said, '... the inadequate instruments and techniques of the past and the intuitive processes of the human mind, so freely brought into play in the interpretation of this type of microseismic data, has reduced the bulk of the work into nothing but history. Only during the past 15 years, have seismologists really come to grips with the geophysics of the problem.' The history of the subject is itself an absorbing study, and those interested may refer to several reviews [*Iyer, 1964; Darbyshire, 1962; Gutenberg, 1958*].

¹ Lamont Geological Observatory, Contribution 1350.

Copyright © 1969 by the American Geophysical Union.

The recent progress in the field may be attributed to the following advances: (1) the replacement of the empirical approach with an abstract model of the earth noise (a stationary, normally distributed, random process), (2) the development of statistical and numerical techniques of data analysis to obtain the meaningful parameters of such a model, and (3) the construction of large arrays of seismometers to permit detailed spatial sampling of the process. The last is a most important advance since it adds two dimensions to the measurement of the earth noise. The topic of this work is the analysis and interpretation of data from the LASA array located in eastern Montana.

Our intent is to describe, quantitatively, wherever possible, the structure of the low-level earth motion, the geographical location of the dominant sources, and the relative importance of possible generating mechanisms. Section 2 describes the data and sample sets used. Section 3 is an outline of the data analysis procedure. In section 4, we introduce the spectrum, showing examples of the frequency and wave-number structure of seismic noise. Section 5 describes the modal structure of the noise, presenting results of the observed diagnostic diagram. Section 6 investigates the different sources for body and surface waves. Body wave sources are located by the range and directional characteristics of the noise. Surface waves are studied by using both single and time-averaged directional results.

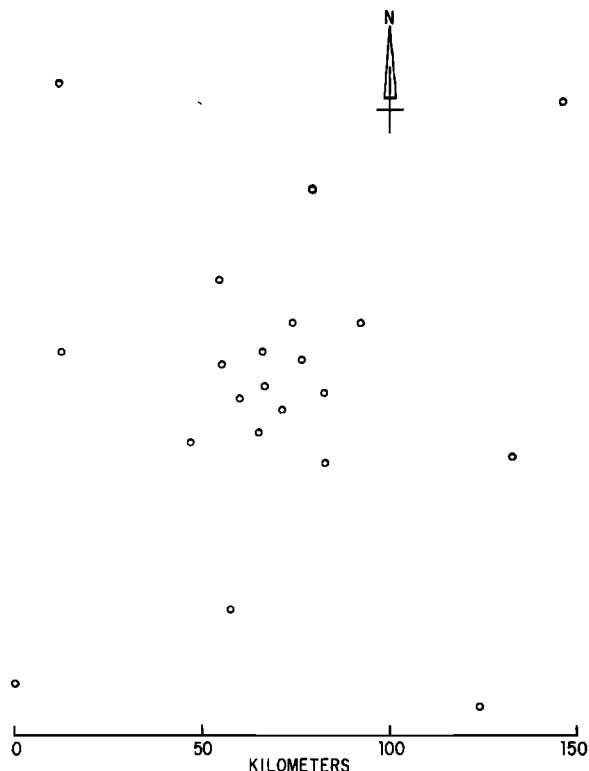


Fig. 1. The 21-point LASA array.

TABLE 1. The Recorded Output of the Array for a Period of about One Hour

Sample Set	Date	Time, UT	Instruments	Frequency Band, mHz	Figure Numbers
1	November 14, 1966	1938-2041	LFV	59-156	9, 10, 11, 28A, 28A'
			LFH	59-200	17, 18
2	January 4, 1967	1200-1251	LFV	59-156	28A, 28A'
3	January 5, 1967	1500-1551	LFV	59-156	28A, 28A'
4	January 6, 1967	2100-2151	LFV	59-156	28A, 28A'
5	January 19, 1967	0550-0654	LFV	59-156	9, 10, 11, 28A, 28A'
			LFH	59-200	17, 18
6	January 26, 1967	1328-1433	LFV	59-156	9, 10, 11, 28A, 28A'
			LFH	59-156	17, 18
7	January 28, 1967	0340-0440	LFV	59-156	9, 10, 11, 28A'
			LFH	59-156	17, 18
8	April 28, 1967	1810-1931	LFV	49-156	9, 10, 11, 28A'
			LFH	49-200	17, 18
9	May 24, 1967	1300-1351	LFV	59-156	28A, 28A'
10	May 26, 1967	0600-0651	LFV	59-156	28A, 28A'
11	May 29, 1967	1300-1351	LFV	59-156	28A, 28A'
12	May 30, 1967	0500-0551	LFV	59-156	28A, 28A'
13	May 31, 1967	2000-2051	LFV	59-156	28A, 28A'
14	September 10, 1967	0842-1002	LFV 17	59-93	28A
			HF	122-312	9, 10, 11, 28A', 28B
15	September 11, 1967	0842-1002	HF	122-312	9, 10, 11, 28A', 28B
16	September 12, 1967	0842-1002	HF	122-195	28A', 28B
17	September 14, 1967	0806-0926	HF	122-195	28A', 28B
18	September 16, 1967	2027-2147	LFV 17	59-93	28A
			HF	122-312	9, 10, 11, 28A', 28B
19	September 18, 1967	2035-2155	LFV 17	59-93	28A
			HF	122-312	9, 10, 11, 28A', 28B
20	September 20, 1967	0601-0721	LFV 17	59-93	
			HF	122-312	9, 10, 11, 28A', 28B

2. DATA

The 21-point pattern of the LASA array is shown in Figure 1. Each point is the center of a subarray of 25 high-frequency vertical seismometers arranged on circles up to $3\frac{1}{2}$ km in radius. In addition, there are 3 low-frequency seismometers, one vertical and two horizontal, at each of the 21 points of the array. Details of the instrumentation are given by *Forbes et al.* [1965].

Both the high-frequency and low-frequency outputs from the LASA seismometers are recorded digitally on the same magnetic tape. The low-frequency components are sampled at 5 times per second; the 25 high-frequency components for each subarray are first summed and then sampled at 20 times per second. Because of the instrumental response of the two different types of seismometers, we have used the low-frequency data to study the band from about 30 to 150 mHz and the high-frequency data to study the band from about 120 to 400 mHz. The data were preprocessed for analysis by detecting and correcting errors followed by digital low-pass filtering and decimation to a sample rate of $1\frac{1}{4}$ samples per second.

The recorded output of the array for a period of about 1 hour makes up a sample set. Table 1 lists the parameters of the sample sets used in the present study. Time average characteristics were obtained by averaging results from several sample sets. The numbers of figures containing time-averaged results are listed in the last column of Table 1 for each sample set. The first column indicates which sample sets were used in each averaged result. After July 1967, the low-frequency instruments from the 4 points on the innermost ring of LASA were removed. Consequently, some of the LF sample sets are from the remaining 17-point array, designated in Table 1 as LFV 17.

3. DATA ANALYSIS

3.1. *The wave-number spectrum.* We assume that the ground motion is stationary in time and space. The practical implication is that second-order statistics do not vary appreciably during the time of one record or over the area of the array. The purpose of the data analysis is to filter data from the LASA array to separate propagating waves by frequency, phase speed, and direction of travel.

Averaging was done in time and frequency to obtain the highest resolution in wave number. The first step was to compute the normalized cross spectrum estimates for each pair of points in the array. Let

$$\mathbf{d}_n; \quad n = 1, 2, \dots, N$$

be the position vectors of an N point array. The coarray corresponding to the set \mathbf{d}_n is given by the points

$$\mathbf{r}_i = \mathbf{d}_n - \mathbf{d}_s; \quad n = 1, 2, \dots, N \\ s = 1, 2, \dots, N$$

which is the set of all vector spacings between pairs of points in the array. For each point \mathbf{r}_i in the coarray, the quantity

$$R(\mathbf{r}_i, f) = \frac{\langle X_{n_f} \cdot X_{s_f}^* \rangle}{(\langle |X_{n_f}|^2 \rangle \langle |X_{s_f}|^2 \rangle)^{1/2}} \quad (1)$$

is the normalized cross spectrum estimate for a narrow frequency band centered at f . The angle brackets $\langle \rangle$ represent averaging of products of the digital Fourier transforms X_{n_f} over both frequency and time. $X_{n_f}^*$ is the complex conjugate of X_{n_f} .

The method of averaging is to break the time series for each array point n

$$x_{nt}; \quad n = 1, 2, \dots, N; \quad t = 0, 1, \dots, T - 1$$

into P equal sections of length $M = T/P$. Call these $x_{n\tau t}$; $\tau = 1, 2, \dots, P$; $t = 0, 1, \dots, M - 1$. For each value of τ , compute the digital Fourier transform

$$X_{n\tau l} = \frac{1}{M} \sum_{t=0}^{M-1} x_{n\tau t} e^{-i(2\pi/M)lt}$$

and average over time and frequency to obtain

$$\langle X_{n_f} \cdot X_{s_f}^* \rangle = \sum_{\tau=1}^P \sum_{l=l_1}^{l_2} C(l) X_{n\tau l} \cdot X_{s\tau l}^*$$

where $f = 2\pi/M [(l_2 - l_1)/2]$ cycles per sample interval. $C(l)$ is a weighting function for averaging in frequency. An example of parameters used is

$$\begin{aligned} l_2 - l_1 &= 6 \\ C(l) &= \frac{1}{18} (l + 1 - l_1); \quad l = l_1, l_1 + 1, l_1 + 2, l_1 + 3 \\ &= \frac{1}{18} (l_2 - l); \quad l = l_2 - 2, l_2 - 1, l_2 \\ &= 0; \quad \text{otherwise} \\ T &= 5120 \quad \text{samples at 0.8-sec intervals} \\ M &= 1024 \end{aligned}$$

which gives estimates with a bandwidth of about 5 mHz and spectrum stability corresponding to about 40 degrees of freedom.

The wave-number spectrum is computed from the cross spectrum estimates

$$S(\mathbf{k}) = \sum_j w_j R(\mathbf{r}_j) e^{-i2\pi\mathbf{k}\cdot\mathbf{r}_j} \quad (2)$$

where \mathbf{k} is the wave-number vector. Equation 2 holds for any value of f ; we therefore drop the f from the notation. The sum on j is over all points in the coarray. The set of weights w_j are chosen to optimize the resolution of the wave-number spectrum window

$$H(\mathbf{k}) = \sum_j w_j e^{-i2\pi\mathbf{k}\cdot\mathbf{r}_j} \quad (3)$$

By using the method of *Haubrich* [1968], the 441 weights w_j were found for the LASA 21-point array that gave the best fit of $H(\mathbf{k})$ to an ideal window of the form

$$\begin{aligned} \mathcal{F}(\mathbf{k}) &= 1, \quad 0 \leq |\mathbf{k}| \leq 1 \\ \mathcal{F}(\mathbf{k}) &= 0, \quad 1 \leq |\mathbf{k}| \leq 100 \end{aligned}$$

where $|\mathbf{k}|$ is in units of millicycles per kilometer.

Figure 2 shows the spectrum window $H(\mathbf{k})$ for the case where all the weights w_j are the same. Wave-number analysis methods using phase, sum, and multiply produce the equal weight window. Figure 3 shows $H(\mathbf{k})$ for the set of weights found by the best fit procedure. The fitted weights result in a spectrum window with significantly narrower main lobe and less side lobe strength.

The use of the normalized cross spectrum, equation 1, results in a wave-number spectrum estimate, equation 2, which is normalized so that, if all the power near a frequency f is concentrated in a sharp wave-number peak, the peak value of $S(\mathbf{k})$ is 1.0 (zero decibel). The effect of this normalization is equalization of the frequency spectrum. The wave-number spectrum results in this paper are in power units normalized in this way.

3.2 The Hankel spectrum. It is often convenient to exhibit the two-dimensional wave-number spectrum in terms of the one-dimensional components of the vector \mathbf{k} . Let r_i , θ_i , and k , α be the polar components of the vectors \mathbf{r}_i and \mathbf{k} . Equation 2 becomes

$$S(k, \alpha) = \sum_j w_j R(r_i, \theta_i) \exp [-i2\pi k r_i \cos(\alpha - \theta_i)] \quad (4)$$

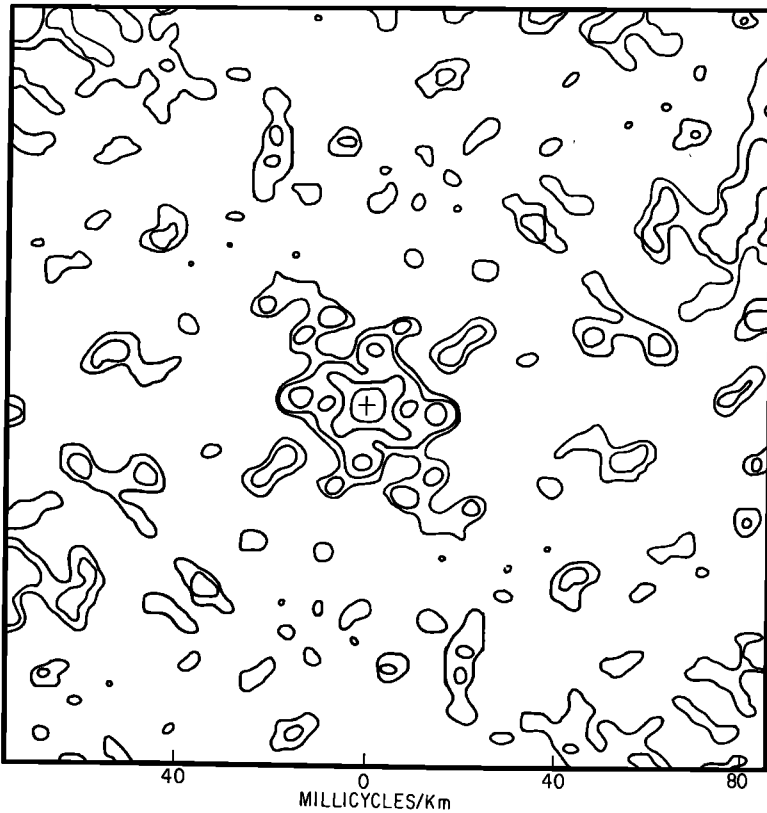


Fig. 2. LASA wave-number spectrum window for equal weights. The center point, marked with a cross, is at zero db; contours are at -3 , -6 , -9 , and -12 db.

Consider the spectrum as a function of k only, independent of α . For this, we use the average of $S(k, \alpha)$ over all α

$$\overline{S(k)} = \frac{1}{2\pi} \int_0^{2\pi} S(k, \alpha) d\alpha$$

and call it the Hankel spectrum. From equation 4

$$\overline{S(k)} = \sum_i w_i R(r_i, \theta_i) \frac{1}{2\pi} \int_0^{2\pi} \exp[-i2\pi k r_i \cos(\alpha - \theta_i)] d\alpha$$

and

$$\overline{S(k)} = \sum_i w_i R(r_i, \theta_i) J_0(2\pi k r_i) \quad (5)$$

follows from the integral representation of the Bessel function $J_0(x)$. The Hankel spectrum is found directly by using equation 5, which is faster to compute than the two-dimensional wave-number spectrum.

3.3. The directional spectrum. The second one-dimensional representation

of the wave-number spectrum is power as a function of propagation direction α . Since different k values correspond to different types of seismic waves, we compute the directional spectrum $S(\alpha)$ from $S(k, \alpha)$ of equation 4 for various fixed values of k . $S(\alpha)$ is thus a one-dimensional function showing the directionality of one kind of wave motion.

It is often useful to average directional spectra in time or frequency to obtain more meaningful and stable results. The frequency averages of $S(\alpha)$ involve choosing a different fixed k for each frequency in order to follow the dispersion curve for the particular wave type being investigated. Time averaging involves averaging directional spectra of a given wave type over different sample sets.

3.4. The radial and transverse spectrum. In section 5, we separate Rayleigh and Love modes by resolving the horizontal ground motion into its radial R and transverse T components.

Let X_n and Y_n be the digital Fourier transforms (at some frequency f) for the east and north components of ground motion at array point n . For propagation in the direction α , the radial and transverse components are given by

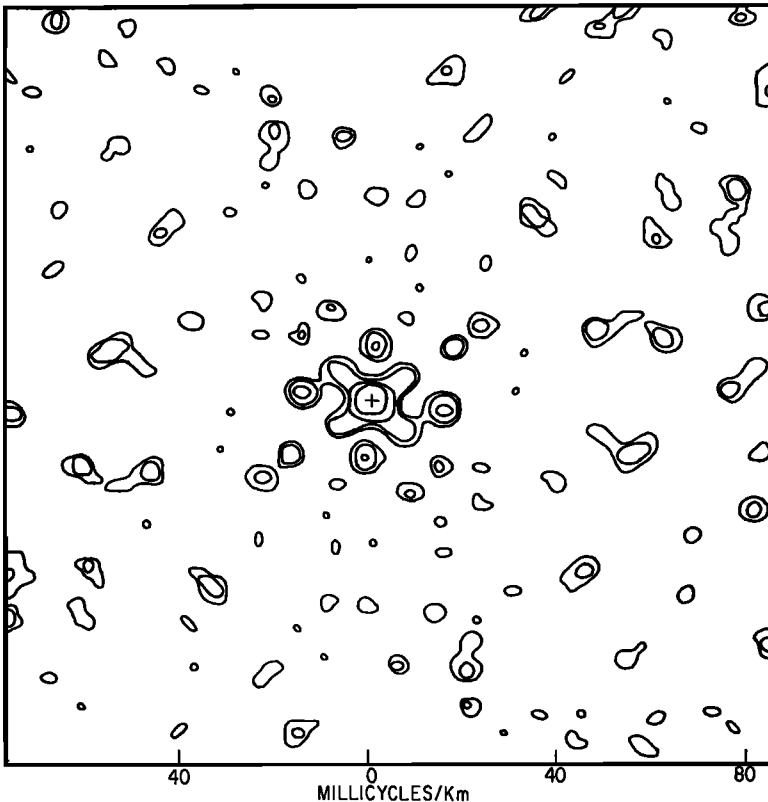


Fig. 3. LASA wave-number spectrum window for fitted weights. The center point, marked with a cross, is at zero db; contours are at -3 , -6 , -9 , and -12 db.

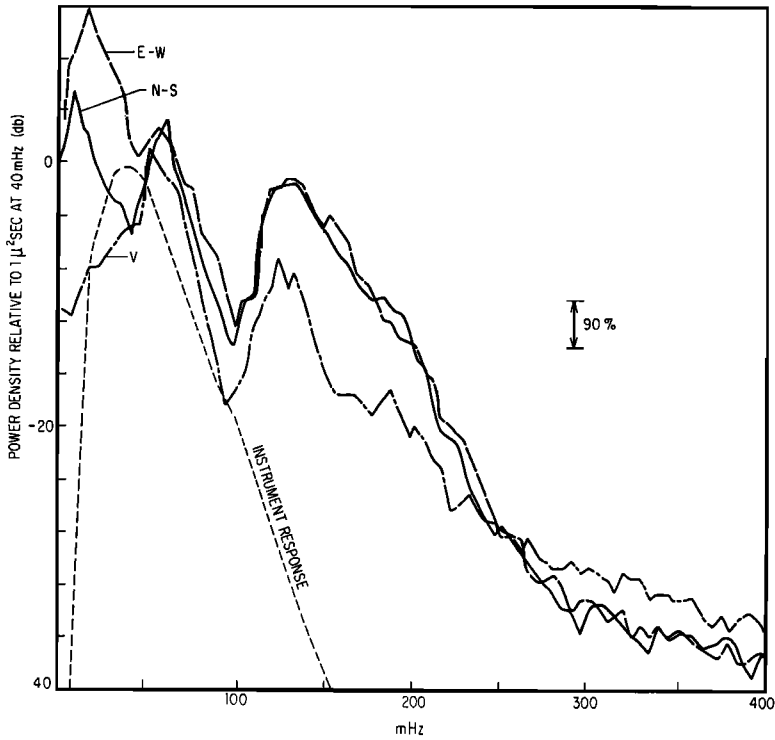


Fig. 4. Representative spectra of vertical, V ; north-south, $N-S$; and east-west, $E-W$; low-frequency instruments at the center point of LASA, sample $S1$.

$$\begin{aligned} X_n \cos \alpha + Y_n \sin \alpha; & \quad \text{radial} \\ -X_n \sin \alpha + Y_n \cos \alpha; & \quad \text{transverse} \end{aligned}$$

The normalized cross spectrum between each pair of array points n and s is

$$R_1(r_i) = 2 \frac{\langle X_n X_s^* \rangle \cos^2 \alpha + \langle Y_n Y_s^* \rangle \sin^2 \alpha + \langle X_n Y_s^* + Y_n X_s^* \rangle \sin \alpha \cos \alpha}{([\langle X_n^2 \rangle + \langle Y_n^2 \rangle] \cdot [\langle X_s^2 \rangle + \langle Y_s^2 \rangle])^{1/2}} \quad (6)$$

for the radial component, and

$$R_2(r_i) = 2 \frac{\langle X_n X_s^* \rangle \sin^2 \alpha + \langle Y_n Y_s^* \rangle \cos^2 \alpha - \langle X_n Y_s^* + Y_n X_s^* \rangle \sin \alpha \cos \alpha}{([\langle X_n^2 \rangle + \langle Y_n^2 \rangle] \cdot [\langle X_s^2 \rangle + \langle Y_s^2 \rangle])^{1/2}} \quad (7)$$

for the transverse component. The radial or transverse wave-number spectrum is found from equation 2 by using $R_1(r_i)$ or $R_2(r_i)$ in place of $R(r_i)$. The normalization in equations 6 and 7 is such that equal radial and transverse power concentrated at one point in the wave-number plane produces a spectrum of one (zero decibel) for both R and T .

3.5. *Stability of estimates.* The statistical fluctuations of wave-number estimates depend on the statistical stability of the cross spectrum estimates used in

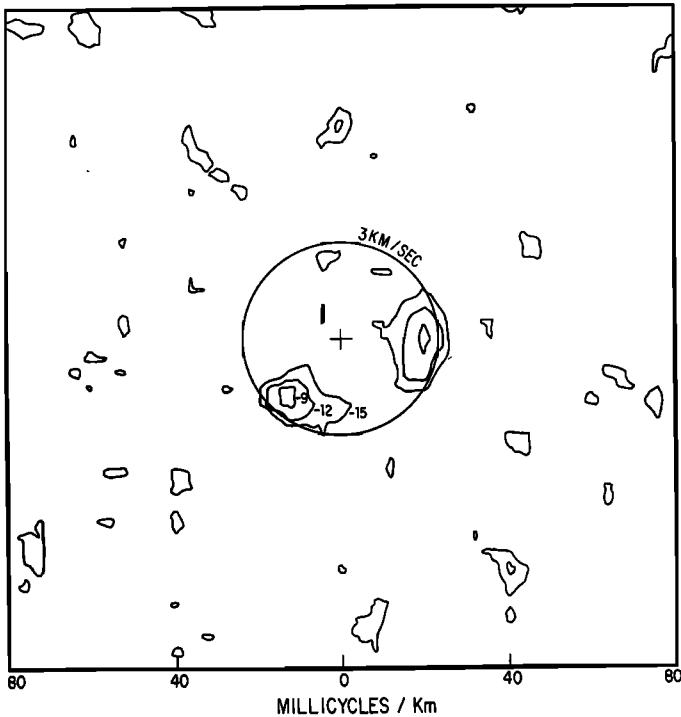


Fig. 5. Wave-number spectrum of vertical motion at 68 MHz, sample S1.

calculating $S(\mathbf{k})$. We have used a Monte Carlo approach to estimate the stability of $S(\mathbf{k})$ estimates for the case where (1) the set of time series recorded from the array are assumed to be independently normally distributed, (2) the cross spectrum estimates $R(r_i)$ are each computed with 40 degrees of freedom, and (3) $S(\mathbf{k})$ is estimated by equation (2) using the fitted weights w_i .

Independent random Gaussian numbers were generated on a computer and used to form 21 time series. $S(\mathbf{k})$ was computed for 8 different frequencies by using the random numbers in place of LASA data. For each frequency, 49 values of $S(\mathbf{k})$ were obtained for \mathbf{k} values on a square grid at 10 millicycles/km spacing centered at $\mathbf{k} = 0$. From the $49 \times 8 = 392$ estimates, a histogram was formed.

To find the expected value of $S(\mathbf{k})$ for random data, we note that the expected value of the cross spectrum estimate $R(r_i)$ is zero except at $r_i = 0$. Thus, using equation 2, the expected value of $S(\mathbf{k})$ is

$$\begin{aligned} E[S(\mathbf{k})] &= \sum_i w_i E[R(r_i)] \exp(-i2\pi\mathbf{k} \cdot \mathbf{r}_i) \\ &= 21w_0 = 6.05 \times 10^{-3} = -22.2 \text{ decibel} \end{aligned}$$

where w_0 is the weight for $r_i = 0$. The variance from the mean was estimated from the histogram of $S(\mathbf{k})$ estimates. It was found that 5% of the estimates exceeded -16.0 decibel. Power values above this level should therefore be significant on

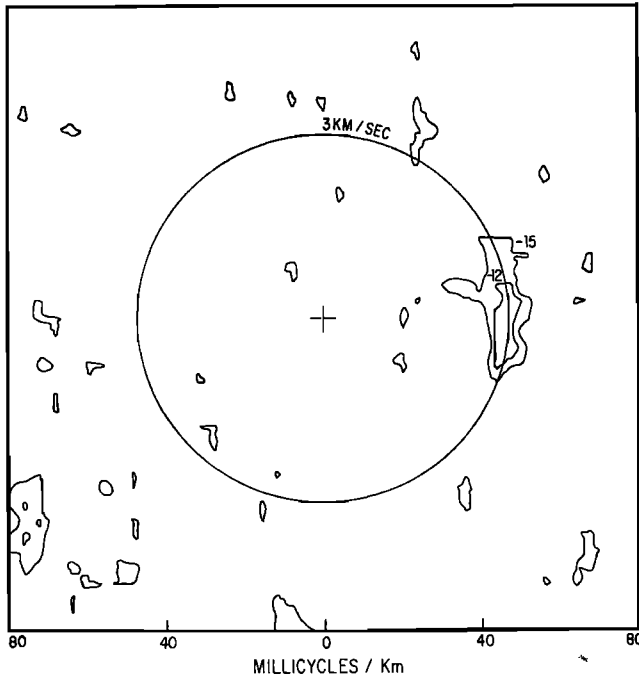


Fig. 6. Wave-number spectrum of vertical motion at 142 mHz, sample S1.

the 95% level. We have used -15.0 decibel as the lowest contour for wave-number spectrum results. In several cases, directional spectra have been averaged over many frequency bands; the variance due to random scatter in these results should decrease in proportion to the number of frequency bands averaged.

4. THE SPECTRUM

Figure 4 shows an example of the vertical and horizontal frequency spectrum computed from a low-frequency sample at the center station of LASA. The two peaks between 50 and 100 mHz and between 100 and 200 mHz are persistent features of the seismic noise [Haubrich, 1967]. We call the lower band PF (primary frequency) and the upper one DF (double frequency). Taking into account the instrument response, we see that the DF peak dominates the spectrum; this peak represents the classical 7-sec microseisms.

Figures 5, 6, and 7 are examples of wave-number spectra $S(\mathbf{k})$ for three different frequency bands 5 mHz wide. Power is contoured in intervals of 3 decibels. The wave-number vector \mathbf{k} is represented by the vector from the origin (marked with a cross) to each point of the figure. Waves propagating north are above and waves propagating east are to the right. Phase velocity is inversely proportional to distance from the origin; circles of constant phase velocity equal to 3.0 km/sec are shown.

Figure 5 is at a frequency centered in the PF band. It shows most of the power concentrated in two peaks traveling east and southwest at a phase velocity

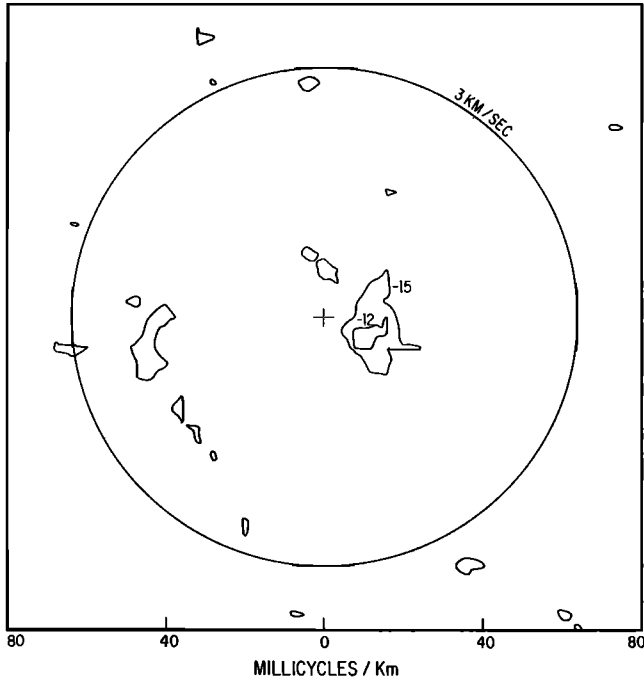


Fig. 7. Wave-number spectrum of vertical motion at 190 mHz, sample S18.

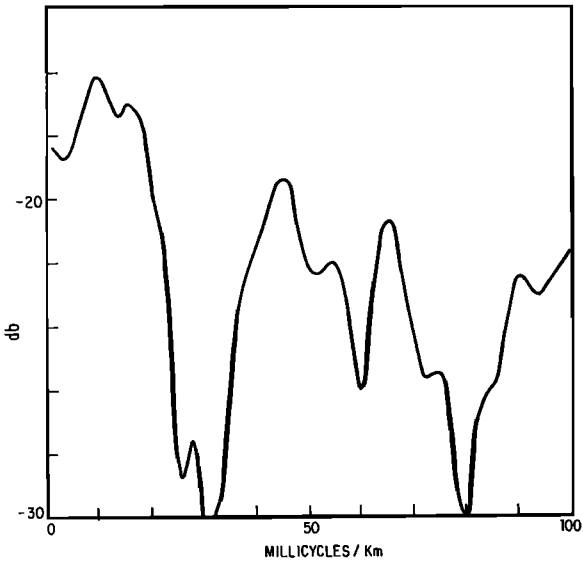


Fig. 8. Hankel spectrum of vertical motion at 190 mHz, sample S18.

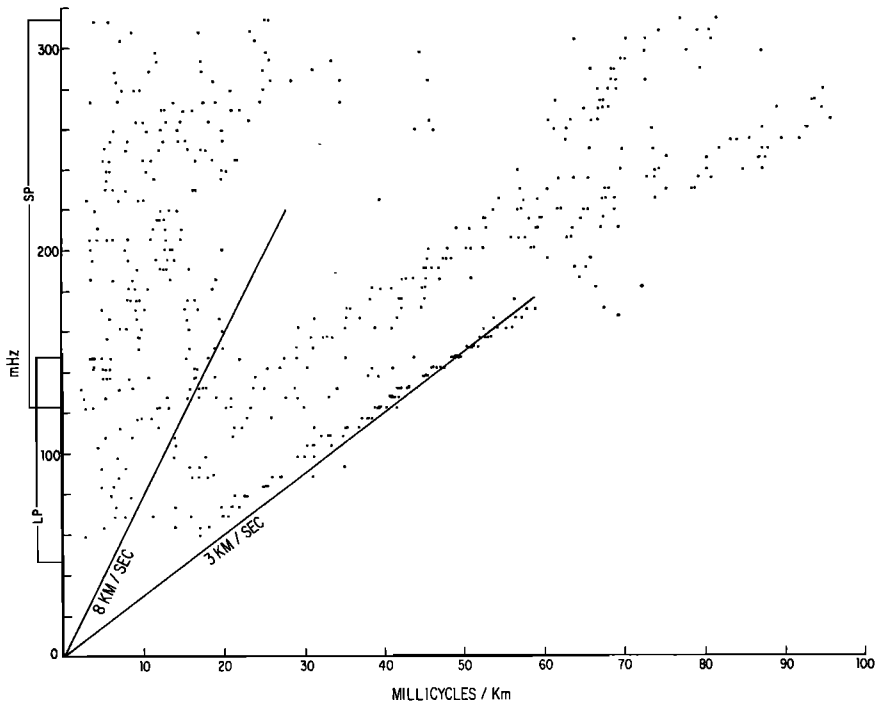


Fig. 9. Frequency wave-number diagram of prominent spectrum peaks for vertical motion for 10 sample days.

somewhat above 3.0 km/sec. The DF band (Figure 6) example shows mostly eastward propagation at about 3.0 km/sec. Figure 7 at 190 mHz, in contrast to the previous two cases, peaks at phase velocities above 10 km/sec. A secondary concentration of power occurs at about 4.2 km/sec for propagation toward the west and southwest.

5. MODES

5.1. Vertical motion. From previous observations of classical microseisms in the DF band centered at 140 mHz, we conclude that an appreciable amount of the motion consists of propagating surface waves of the Rayleigh type [Darbyshire, 1954]. Rayleigh waves in the microseisms could be recognized from the 90° phase shift between vertical and horizontal motion. For a single narrow directional beam of Rayleigh waves, the coherence between vertical and horizontal motion is high, and the 90° phase shift is good diagnostic evidence for Rayleigh motion. For the more general case of broad-beam propagation, the coherence is low and the phase difference is not necessarily meaningful. Data from the LASA low-frequency three-component instruments show the Rayleigh 90° phase shift in the PF and DF bands for narrow-beam propagation.

The mode structure of the seismic noise at LASA was investigated by obtaining an observed diagnostic diagram, power as a function of wave number, $k = |\mathbf{k}|$, and frequency f . The Hankel spectrum $\bar{S}(k)$ was first computed for several dif-

ferent frequencies and sample sets. Figure 8 is an example of $\overline{S(k)}$ for a 5-mHz frequency band at 190 mHz; it is the directional average of the wave-number spectrum shown in Figure 7. Because of directional averaging, the Hankel spectrum gives a more stable and detailed picture of power as a function of k . Figure 8 shows three principal features: (1) a broad concentration of power at low wave number, the body wave propagation; (2) a peak near 45 millicycles/km, which is interpreted

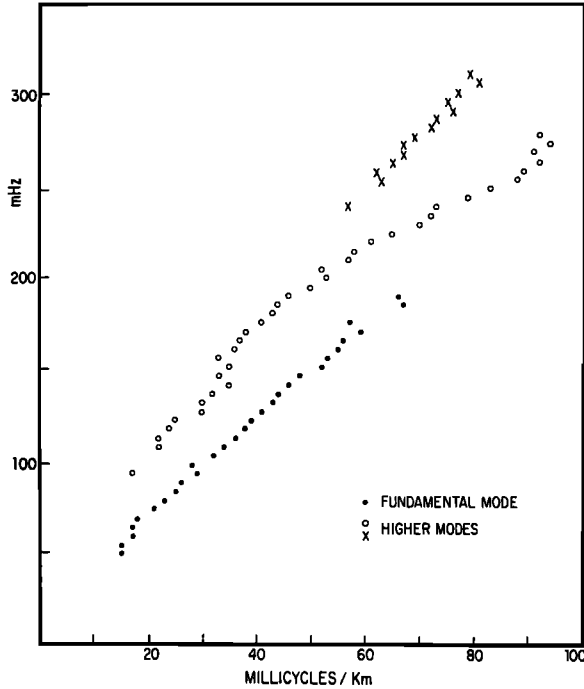


Fig. 10. Time-averaged frequency wave-number diagram for vertical fundamental and higher Rayleigh modes.

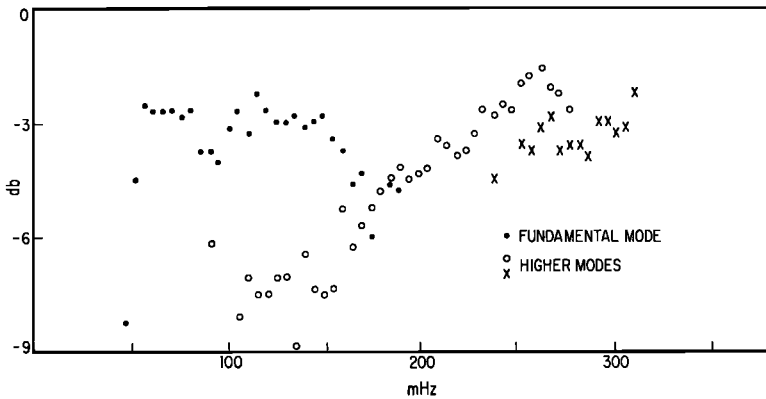


Fig. 11. Time-averaged power versus frequency for vertical fundamental and higher Rayleigh modes.

as a higher Rayleigh mode; and (3) a peak near 65 millicycles/km, the fundamental Rayleigh mode. This last peak is not evident on the wave-number spectrum but is brought out by the directional averaging.

The concentration of power in the trapped modes is a function of the geologic structure underneath the LASA array. If the structure is sufficiently inhomogeneous, we might expect the diagnostic diagram to be a function of direction. If such directional differences exist, they are not obvious in our results at the wave-number resolution and in the frequency bands investigated.

Power as a function of f and k is shown in Figure 9 for data from ten sample sets (see Table 1). Only the two or three most prominent peaks of $\overline{S}(k)$ are plotted as points in the figure. The close concentration of points near the 3-km/sec phase velocity trace out the dispersion curve for fundamental Rayleigh waves. Above the Rayleigh mode the points are more scattered but are still concentrated along a curve, showing the presence of a higher mode. Above 200 mHz the data suggest that at least two higher modes are present.

In the low wave-number region of the figure at phase velocities above 8 km/sec, the peak power points show no clear pattern. In particular there is no obvious continuation of the trapped mode lines into the low wave-number region.

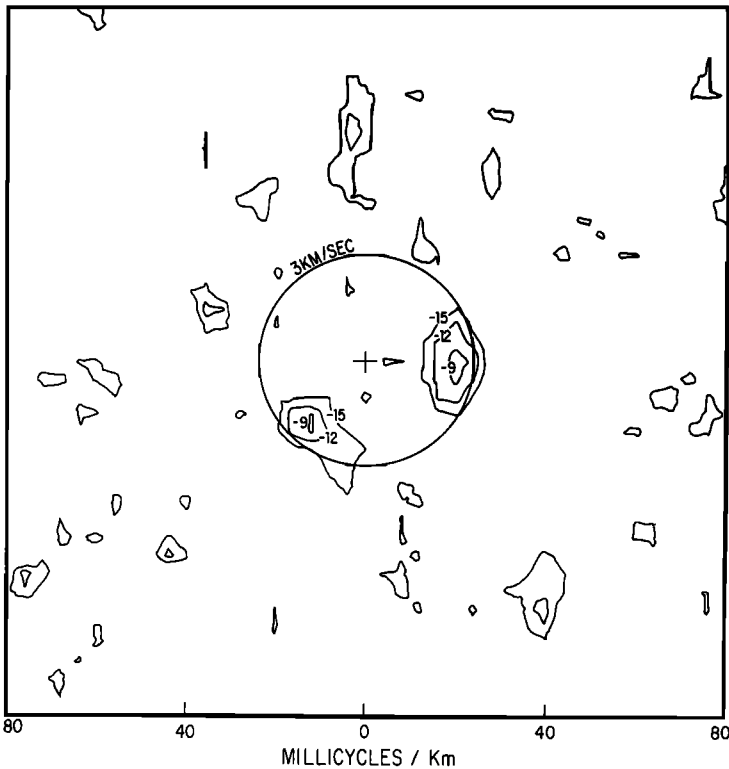


Fig. 12. Wave-number spectrum of horizontal radial motion at 68 mHz, sample S1.

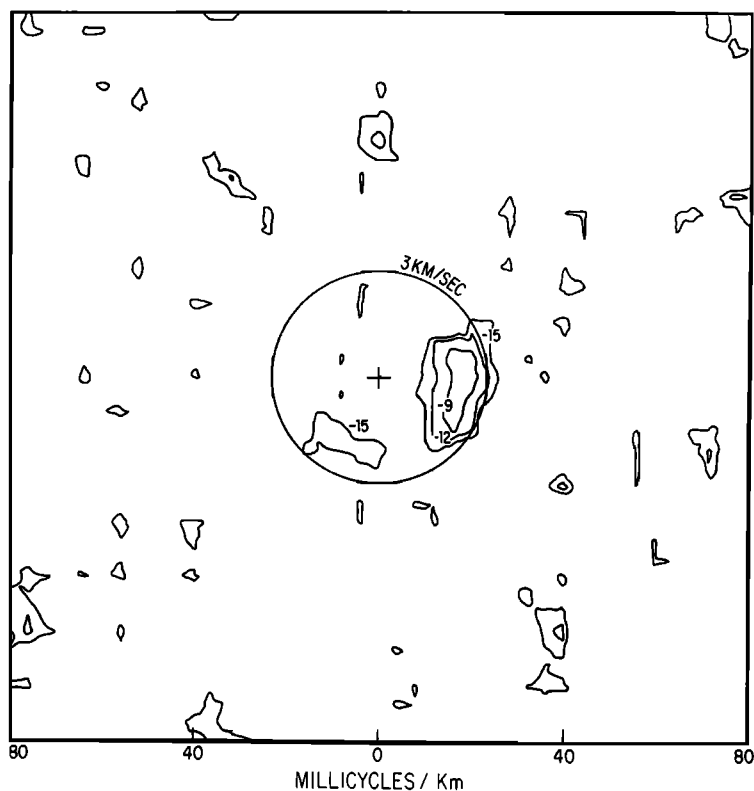


Fig. 13. Wave-number spectrum of horizontal transverse motion at 68 mHz, sample S1.

The body wave phase velocities appear to be controlled by the properties of their sources; this will be discussed in section 6.

The scatter in Figure 9, especially for points representing the higher modes, is no doubt due to statistical fluctuations in the spectrum estimates. There is considerable variation in the higher mode power from one day to the next, and low power peaks will not be as significant as high power peaks. We have therefore averaged the data of Figure 9 over the different sample sets (time averaging) to obtain better estimates of the dispersion curves. For each frequency band the peak k values for different sample sets were weighted by their normalized power before averaging. Figure 10 shows the time-averaged plot of the peak power as a function of f and k for the data of Figure 9. The results are our best estimates of the dispersion curves for the three Rayleigh modes occurring in the seismic noise.

Figure 11 shows the average power versus frequency for the modes shown in Figure 10. It should be noted that the power is relative to each frequency band, the frequency spectrum having been equalized as described in section 3.1. The results show that above the frequency of the classical microseisms (150 mHz) the fundamental mode power begins to fall while the higher mode power

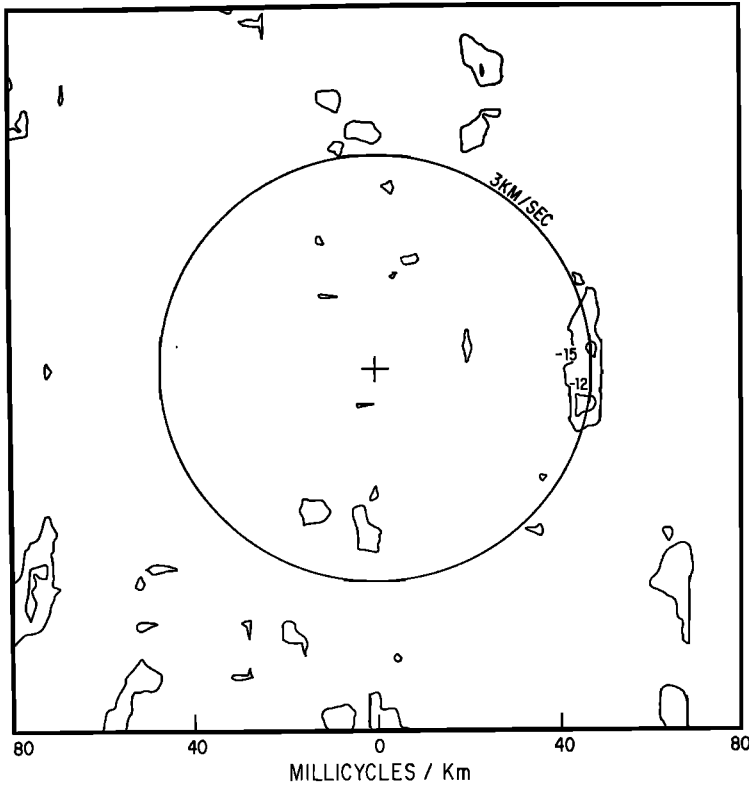


Fig. 14. Wave-number spectrum of horizontal radial motion at 142 mHz, sample S1.

begins to increase; at 200 mHz and above, the higher modes dominate the Rayleigh wave noise.

5.2. Horizontal motion. The observation of horizontal microseisms has raised several questions regarding the nature of the motion. The first concerns the modes of propagation: Do horizontal microseisms propagate as a mixture of Love and Rayleigh modes? If Love modes are present, what is their relative power compared with the Rayleigh motion? Finally, what are the possible sources of the Love motion?

Records from a single three-component station give some indication that Love waves are present in the horizontal motion. The critical observation has been that vertical-to-horizontal coherence is almost always greater than the coherence between the two horizontals. The limited wave-number resolution of a single three-component station leads us to consider only very restricted models of Rayleigh and Love modes. Thus, *Darbyshire* [1954] considered equal amounts of Rayleigh and Love power from a single source, *Iyer* [1959] assumed directed Rayleigh and isotropic Love propagation, and *Darbyshire* [1963] used several models, including the above two and some with broad beam propagation.

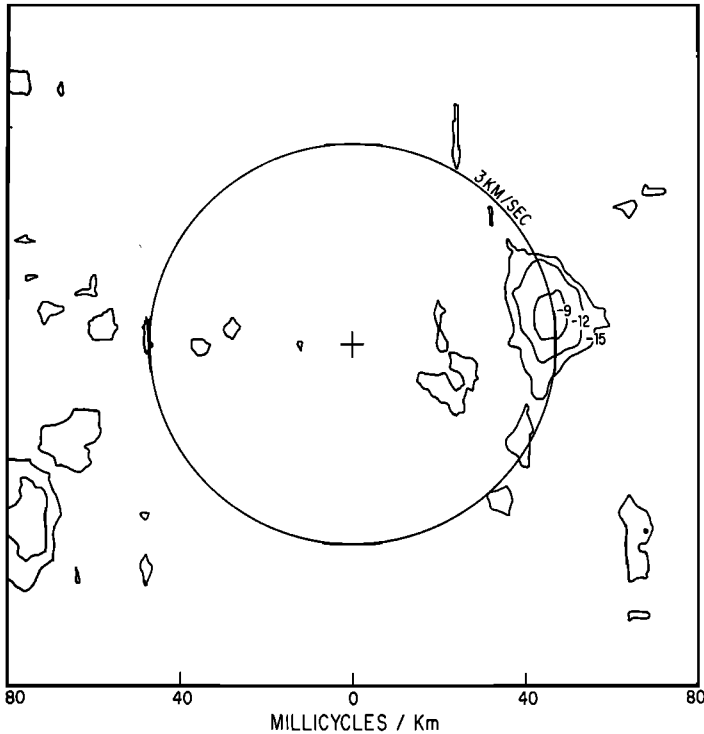


Fig. 15. Wave-number spectrum of horizontal transverse motion at 142 mHz, sample S1.

The 21-station 3-component LASA array allows one to compute the wave-number spectra of horizontal motion and to separate the Rayleigh and Love components. *Toksöz and LaCoss* [1968] made a separation of the horizontal motion into radial R and transverse T for a 'beam' directed toward the main source of energy. They identified the appreciable energies in T as the Love wave component.

We have computed wave-number spectra for the R and T horizontal components by the method outlined in section 3.4 for five different days. Figures 12 and 13 show an example of the wave-number spectrum for R and T at a frequency in the PF band; Figures 14 and 15 are at a frequency in the DF band. The T power is concentrated in peaks in both frequency bands, indicating that transverse horizontal power propagates as a mode from sources in rather well-defined directions.

It is a striking feature of the spectra that the T or Love mode has a directional distribution similar to the R or Rayleigh mode. The directional similarity occurs on all five records analyzed for horizontal motion, which suggests that Love waves are generated near Rayleigh wave sources. The evidence is against local generation of Love waves from some sort of Rayleigh wave conversion.

The wave-number spectra examples show greater transverse wave power

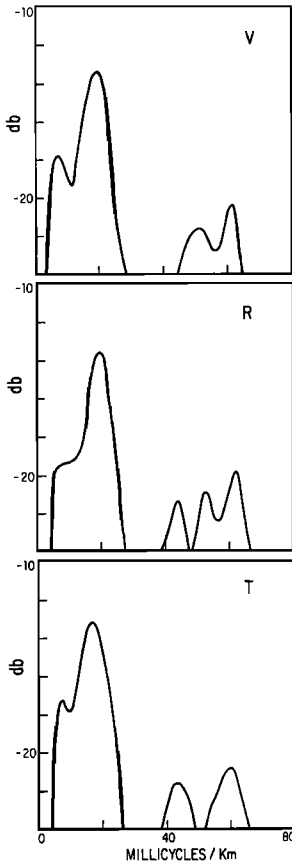


Fig. 16. Hankel spectra of V , vertical motion; R , horizontal radial motion; and T , horizontal transverse motion at 68 mHz, sample S1.

than radial wave power from the eastward propagating waves. The southeastward propagating waves at 68 mHz, however, have greater radial power. For the five different days examined, the transverse wave to radial wave power ratio varied between about 0.5 and 2.0.

The time-averaged properties of the Rayleigh and Love wave parts of the horizontal motion were examined by computing Hankel spectra for the five sample sets at frequencies between 50 and 200 mHz. Figure 16 contains examples of R and T Hankel spectra, showing the power concentration in the Rayleigh and Love modes. The peak power and corresponding k value from the modal peaks were used to find time average power and time average dispersion curves. Figure 17 shows the time-averaged power and power ratio for Rayleigh and Love modes as a function of frequency; there is no clear predominance of Rayleigh or Love waves. The results do suggest, however, a frequency structure to the partition of power in the modes. Below 100 mHz, Love waves predominate; from 100 to 140 mHz and above 170 mHz, Rayleigh waves are strongest.

We might expect the dispersion curves for Rayleigh and Love waves to differ. In fact, the wave-number spectra show that the T component peaks at a slightly lower k value than the corresponding R component. The Hankel spectra

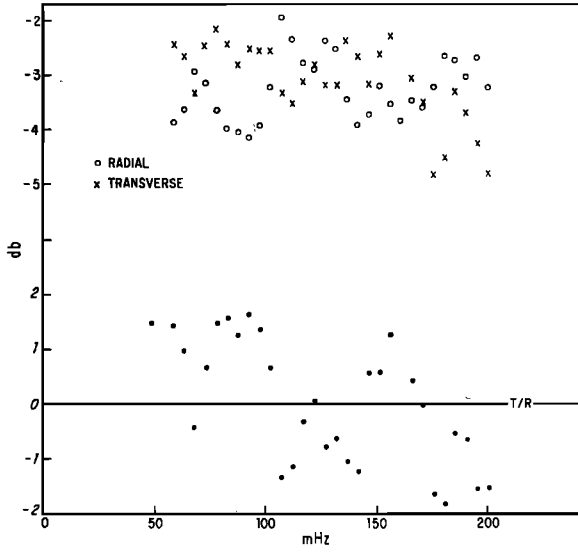


Fig. 17. *Top*: time-averaged power versus frequency of radial and transverse motion. *Bottom*: ratio of time averaged transverse T to time averaged radial R power.

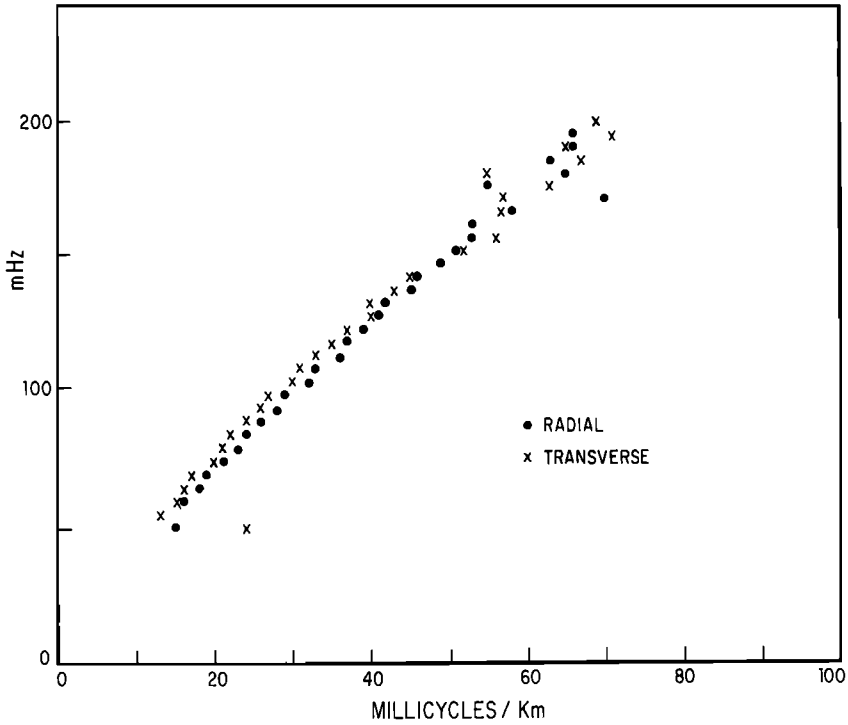


Fig. 18. Time average frequency wave-number diagram for horizontal radial and transverse modes.

in Figure 16 show more clearly the peak k value for R and T . Figure 16 also shows that the R component peaks at the same value as the vertical component, which is consistent with the Rayleigh wave interpretation of R .

Figure 18 shows a time-averaged dispersion curve for the Rayleigh and Love components (R and T). The two modes are clearly separated for frequencies below 150 mHz; the Love waves have a higher phase velocity (lower k) for a given frequency. Above 150 mHz, the results are inconclusive and most likely represent the presence of higher modes that could not be resolved.

6. SOURCES

The 7-sec microseisms make up the peak power in the seismic noise spectrum. They have consequently been the most studied, the earliest observations suggesting ocean waves as sources [Wiechert, 1904].

There are two mechanisms for generating propagating seismic energy from ocean waves that quantitatively explain the observations. The first is nonlinear interaction of oppositely traveling ocean waves as proposed by *Longuet-Higgins* [1950] that produces seismic waves (DF) with double the ocean-wave frequency. The theory as generalized by *Hasselmann* [1963] explains the spectrum peak near 7 sec and agrees quantitatively with seismic and ocean-wave observations. *Abramovici* [1968] has extended the theory to include the generation of leaking compressional modes by the same nonlinear ocean-wave process.

DF seismic noise may be generated in any region of an ocean containing waves of similar frequency moving in opposite directions. Three situations have been proposed [*Longuet-Higgins*, 1952] in which the opposing wave motion may

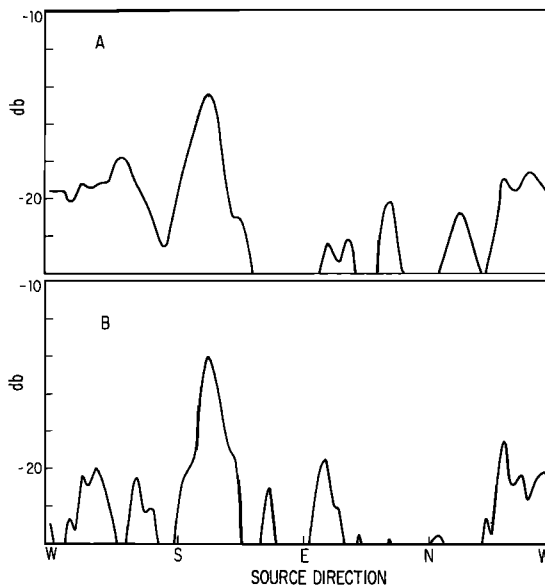


Fig. 19. Broad band directional spectra at phase velocity of 10.2 km/sec for A , 122–313 mHz; for B , 317–508 mHz, sample S20.



Fig. 20. Geographical distribution of body wave source power, 278-313 mHz, sample S14. The contour interval is 1 db. Hurricanes Lily (*L*) and Beulah (*B*) are shown by the solid symbols; tropical storm Doria (*D*) is shown by the open symbol. The shaded area indicates atmospheric pressure less than 996 mb. The map is an azimuthal equidistant projection centered at LASA (the small cross in the center of the figure).

be strong: (1) reflection from a coast, (2) the wake of a moving storm, and (3) the center of a storm. Generation of DF by ocean waves near coastlines has been observed [*Haubrich et al.*, 1963], indicating the first possibility. Other observations [*Iyer*, 1958] have found DF coming from the direction of storms at sea, suggesting the second or third possibilities.

Our purpose is to separate DF seismic noise into its component surface and body modes and to study the possible source locations of each. We wish to obtain a general picture of the dominant geographical distribution of source areas with particular attention to the relative importance of coastline and storm center generation.

The second method of generating seismic waves by oceans, first proposed by *Wiechert* [1904], is the action of ocean waves on coasts. The quantitative theory of this mechanism given by *Hasselmann* [1963] leads to seismic waves (PF) with the same frequency as the ocean waves. The PF seismic noise is gen-



Fig. 21. Geographical distribution of body wave source power, 356-391 mHz, sample S18. The positions of hurricane Chloe (C) on the 2 preceding days are shown by the open circles.

erated in shallow water only; the mechanism favors low frequencies, so that the observed spectrum is typically peaked in the band 60-90 mHz [Oliver and Page, 1963; Oliver, 1962; Haubrich et al., 1963].

The observations of PF at LASA show that the vertical motion consists primarily of the fundamental Rayleigh mode. From the directional distribution of PF, we obtain some indication of the geographical distribution of low-frequency ocean waves.

6.1. *Body waves.* In section 5, it was shown that the seismic noise at LASA includes a significant amount of power above about 150 mHz at compressional wave phase velocities. The directional spectrum $S(\alpha)$ was computed by the method outlined in section 3 to study the location of body wave source areas. $S(\alpha)$ was computed for different fixed values of k corresponding to compressional horizontal phase velocities between 8 and 25 km/sec. The directional spectra were first computed for frequency bands 5 mHz wide. The resulting $S(\alpha)$ values were then averaged over adjacent frequency bands for fixed phase velocity. Figure 19 shows two such frequency-averaged directional spectra for phase velocity $c = 10.2$ km/sec. Each of the wide frequency bands, 122-313 mHz and

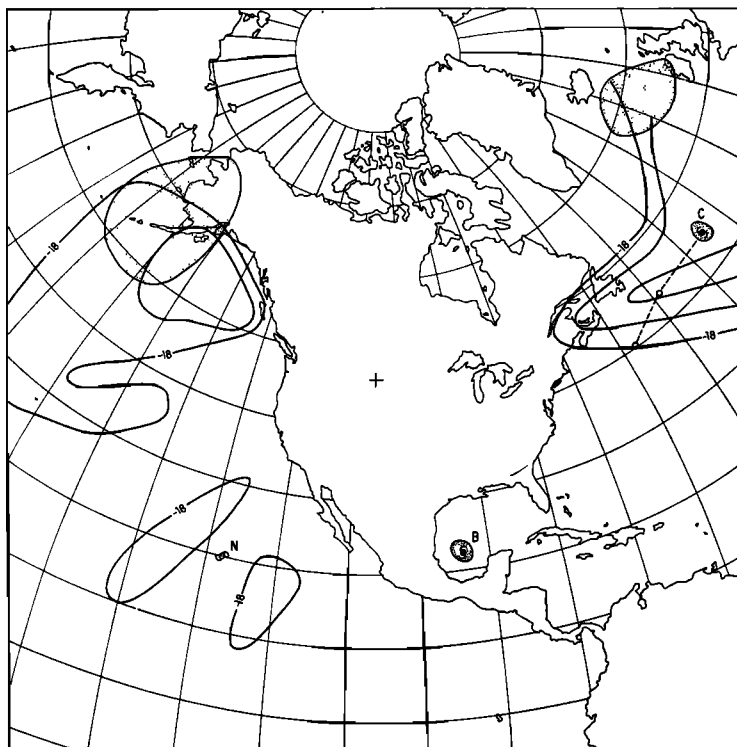


Fig. 22. Geographical distribution of body wave source power, 239–273 mHz, sample S19.

317–508 mHz, were obtained by averaging 40 narrow band results. The peak power in both frequency bands is in the source direction of hurricane Beulah, which was in the Gulf of Mexico at the time of this record.

By using the Jeffreys-Bullen travel time curve, the horizontal phase velocity can be converted to the range of a source from LASA. The phase velocity of 10.2 km/sec corresponds to a range of about 20° , which puts the source of the body wave peak power in the Gulf of Mexico close to the hurricane.

Figures 20 to 24 show the location of sources of body wave power arriving at LASA along with the location of meteorological events for records taken on 4 different days in September 1967. The time spanned by the sample sets includes the occurrence and movement of several tropical hurricanes, storms, and high-latitude frontal systems. The following meteorological events occurred during the 10-day period, September 10–20, 1967: hurricane Lily climaxed off Baja California on September 10; hurricane Beulah moved from the Caribbean south of Puerto Rico into the Gulf of Mexico and struck the shore near Brownsville, Texas; hurricane Chloe moved toward Nova Scotia, turned eastward and, moving quite rapidly, crossed the North Atlantic at about latitude 45°N ; hurricane Doria developed from a tropical storm and expired on Cape Hatteras;

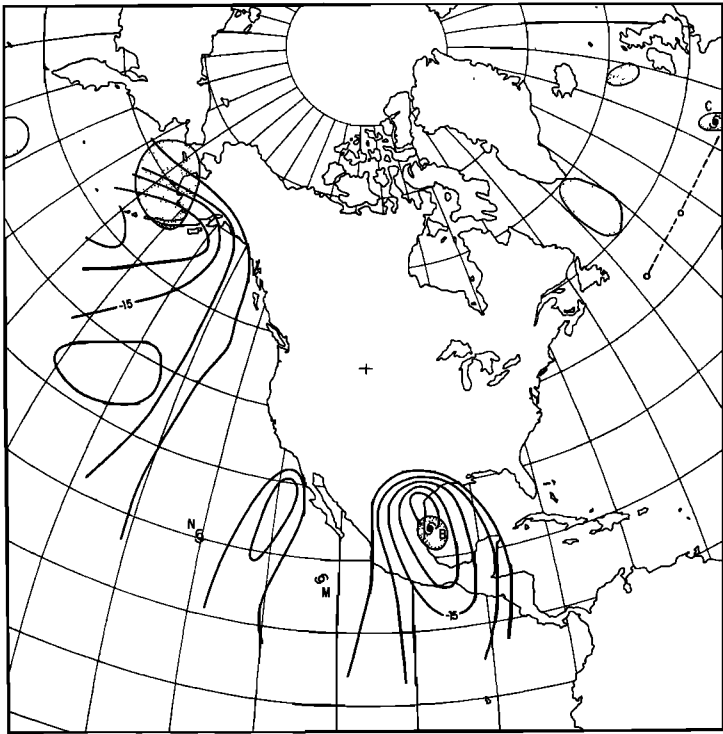


Fig. 23. Geographical distribution of body wave source power, 161-195 mHz, sample S20.

tropical storms Nanette and Monica lingered far off the west coast of Mexico; and several frontal systems occupied the North Atlantic and North Pacific.

The contours on each map show the relative power of compressional wave sources as determined from the directional spectra. The directional spectra at a fixed phase velocity (corresponding to a range) were averaged over eight adjacent frequency bands 5 mHz wide. This frequency-averaged power, computed for a set of different ranges, was contoured on the maps. The maps indicate a clear relationship between well-developed storms and body wave source locations. Hurricanes Lily, Chloe, and Beulah and tropical storm Nanette show the best evidence of body wave generation near the storm centers. The relationship holds even when the storm is located in the open ocean well away from the coast.

Fast moving hurricane Chloe shows a source area that is in the wake of the storm in Figures 21, 22, and 24. This appears to be a case of a storm overriding its own waves. A storm moving at speed V will override its waves for frequencies above a cutoff frequency f_0 , where $f_0 = (g/4\pi V)$ and g is the earth's gravitational acceleration. Waves at frequencies above f_0 will have group velocities slower than the storm velocity. This produces oppositely traveling ocean waves in the wake of the storm. The cutoff frequency for DF seismic waves is $2f_0$. For a storm moving $10^\circ/\text{day}$, the DF cutoff is at about 123 mHz. The mechanism

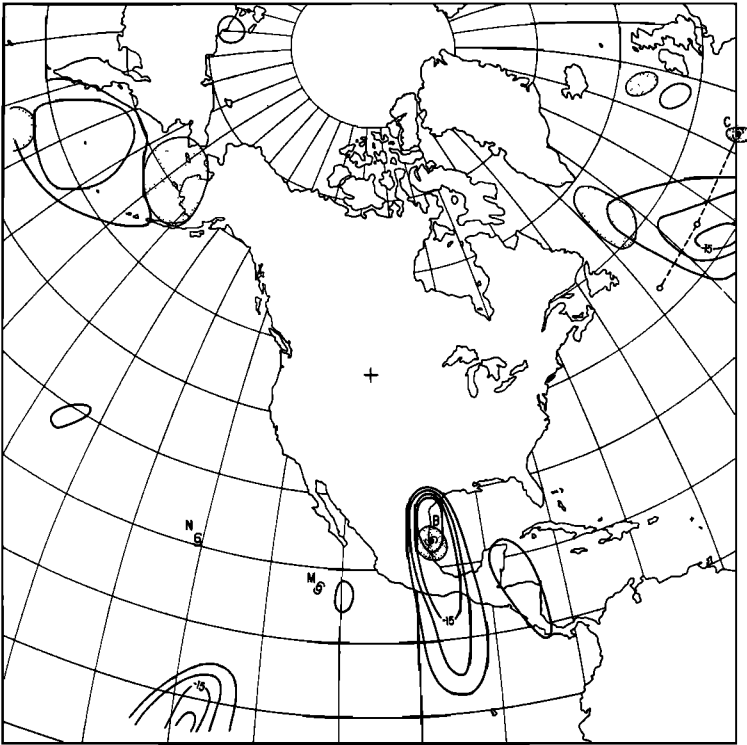


Fig. 24. Geographical distribution of body wave source power, 317-352 mHz, sample S20.

thus favors high-frequency DF generation, and only relatively fast moving storms should generate low-frequency seismic energy.

Figures 23 and 24 show body wave sources for the same sample set but in different frequency bands, centered at 178 and 334 mHz. The body waves from the wake of Chloe show up only in the higher-frequency band. Taking the speed of Chloe to be about $10^\circ/\text{day}$ over the preceding 2 days, the cutoff at 123 mHz is well below the 178-mHz band. Apparently frequencies above but close to the cutoff are still not strongly generated. In fact, a simple model of a moving storm gives a cutoff somewhat above $2f_0$ due to the limited extent of the wake. Consider a point source storm that generates waves isotropically at a uniform rate. The storm at position x moves with constant speed V in the positive x direction (see Figure 25). At the origin, a distance x behind the storm, waves with group velocity $W < V$ will arrive simultaneously from sources at previous positions of the storm x_1 and x_2 , where

$$\frac{x_1}{W} = \frac{x - x_1}{V} \quad \text{and} \quad -\frac{x_2}{W} = \frac{x - x_2}{V}$$

The nonlinear mechanism for generating seismic waves requires two ocean-wave groups that move almost in opposite directions. Thus two wave groups

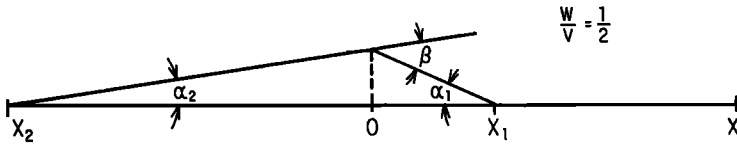


Fig. 25. Geometry of wave interference in the wake of a storm at position x , moving toward the right with velocity V . Waves moving with velocity W , originating at positions x_1 and x_2 , interfere near position 0. Waves moving left within the angle α_1 oppose waves moving right within the angle α_2 , so that their angle of interference is no greater than β .

whose propagation direction differs by more than $180^\circ + \beta$ (where β is a maximum angle of interference) will result in wave-number differences that are larger than the wave number of the corresponding seismic modes. We therefore consider only the wave energy within the angles α_1 from x_1 and α_2 from x_2 , where $\beta = \alpha_1 + \alpha_2$.

Since

$$\begin{aligned}\alpha_1/\alpha_2 &\simeq x_1/x_2 \\ \alpha_1 &= (\beta/2V)(V + W) \\ \alpha_2 &= (\beta/2V)(V - W)\end{aligned}$$

The wave power coming from source x_1 is proportional to $[W/(V + W)]$ times the angle α_1 ; the power from x_2 is proportional to $\alpha_2 [W/(V - W)]$. From the above results we have

$$\alpha_1[W/(V + W)] = \alpha_2[W/(V - W)] = (W\beta/2V)$$

The generation of microseisms as a function of frequency thus depends only on the ocean-wave group velocity W , which is inversely proportional to frequency and reaches its maximum at the cutoff frequency f_0 .

The above result indicates that the interference behind a storm should be greatest at the lowest frequencies just above the cutoff when W almost equals V . In most cases, however, the lowest frequencies above cutoff will not be generated because of a limitation in the size of the generating region. The above equations show that $x_2 = (W/V - W)x$ becomes large for small $V - W$ except at small x .

To explain the lack of significant power from Chloe at 178 mHz, we note that at this frequency $x_2 = 2.2x$, so that interference 10° behind the storm would have to originate 32° behind the storm, a region outside the wake of Chloe. On the other hand, Figure 24 shows body waves from 10° behind Chloe at 339 mHz. For this frequency, $x_2 = 0.59x$, placing the source for interfering waves well within the wake.

The evidence suggests that fast-moving storms produce compressional seismic noise above some lower frequency limit. The lowest-frequency compressional waves may, however, still be generated near coastlines as reflected waves. This is indicated by Figure 23, where energy from both the northwest and from the southwest comes from near the coast in contrast to the situation at higher fre-

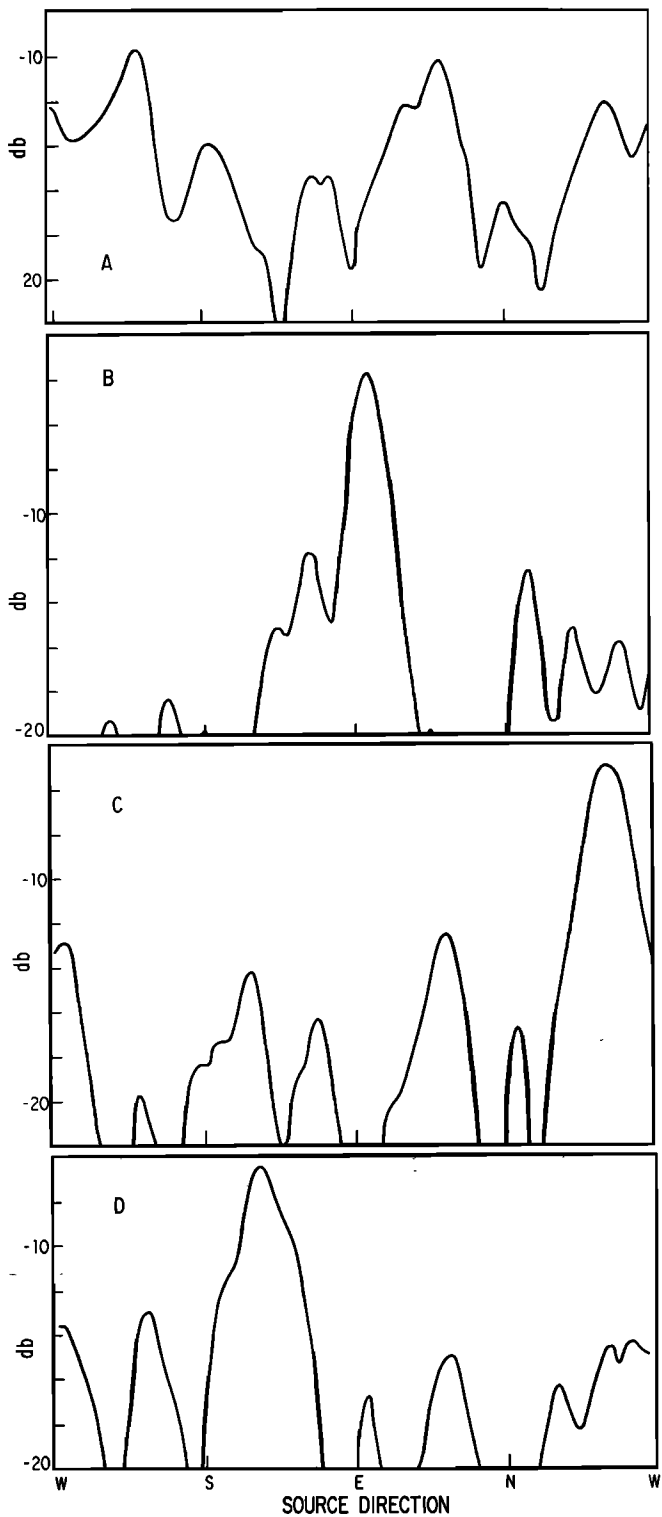


Fig. 26. Directional spectra of PF vertical Rayleigh motion, 59-93 mHz: A, sample S14; B, sample S18; C, sample S19; and D, sample S20.

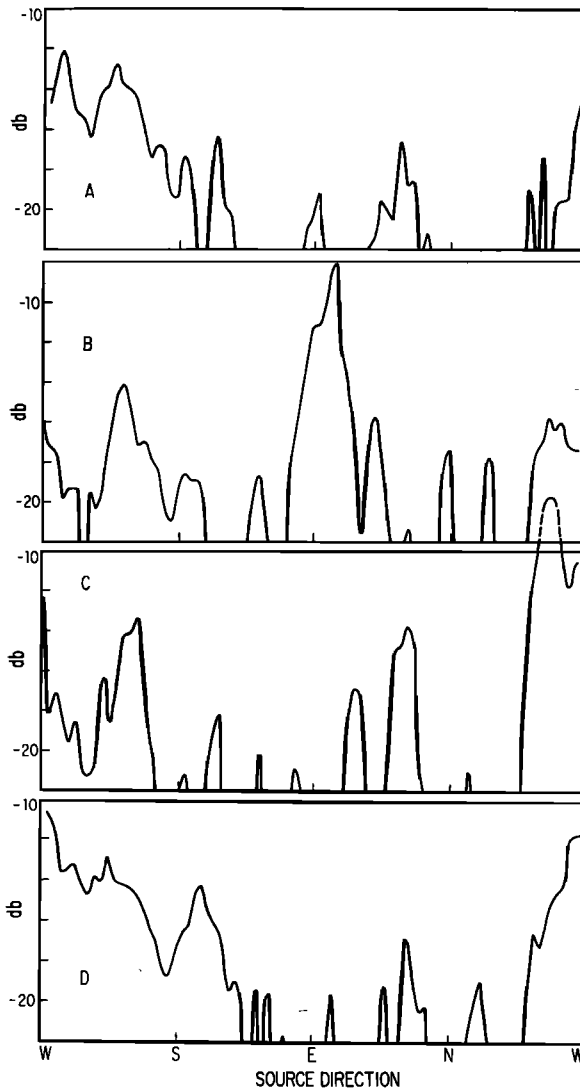


Fig. 27. Directional spectra of DF vertical Rayleigh motion, 122–156 mHz: *A*, sample S14; *B*, sample S18; *C*, sample S19; and *D*, sample S20.

quency (Figure 24). Hurricane Beulah at this time is slow moving and near a coast. The slow speed suggests coastline reflection in both frequency bands.

6.2. *Surface waves.* Sources of surface waves were investigated by first computing directional spectra for frequency bands of 5 mHz at wave numbers corresponding to the vertical fundamental Rayleigh mode. Unlike body waves, surface wave phase velocities do not determine source range.

Frequency-averaged directional spectra were found by averaging the directional spectra from eight adjacent 5-mHz bands for a single sample set. Figures

26 and 27 show frequency-averaged directional spectra for PF in the band 59–93 mHz and DF in the band 122–156 mHz for the sample sets on the same four days that were used in the body wave examples (Figures 20–24).

Some PF source directions should correspond to the location of coastlines near to large storms. This in fact is seen in Figure 26: in curve *A* the power peaks from the southwest, the direction to hurricane Lily; in curve *B* the power is mostly from the direction of hurricane Chloe in the Atlantic; and in curve *D* the greatest power is from the direction of hurricane Beulah in the Gulf of Mexico. On the other hand, PF surface waves can also be generated at coastlines by swell from distant storms [Oliver and Page, 1963; Haubrich et al., 1963]. This type of generation may be the cause of other peaks in the seismic power, such as the one from the northeast in curve *A*, Figure 26.

In Figure 27, curves *A*, *B*, and *D* show that the three storms near coasts that produced peaks in PF also produced peaks in DF. There are significant differences between the two curves: the DF power from the northeast in curve *A* is lower than the corresponding PF, whereas the DF power in curve *D* is high from the northwest to the southwest.

Both the PF and DF power from hurricane Chloe diminishes during the two days between curves *B* and *C* of Figures 26 and 27. The absence of PF power on the later day suggests lower coastal ocean-wave activity. The DF power drops when the coastal PF power drops, and there is no tendency for the DF surface waves to follow the storm. The situation contrasts with the body waves from Chloe (Figures 21 and 22).

The directional spectra for single sample sets show that DF sometimes differs significantly from PF. The difference could be due to one of two causes: (1) DF generation occurs in a part of the ocean far from the coasts where the sea state is different, or (2) time variations in the direction of swell near a coast may be responsible for differences in the relative amounts of PF and DF excitation, even though both are generated by the same swell near a coast.

In an attempt to separate the two situations, we have computed a time-averaged directional spectrum for PF and DF by averaging directional spectra of sample sets from several different days (Table 1). Time averaging should reduce differences due to effect 2. Spectra for the higher Rayleigh modes were computed in a similar way for the frequency band 160–195 mHz at phase velocity 4.4 km/sec.

Time-averaged directional spectra in Figure 28 (curves *A*, *A'*, and *B*) are shown compared with three direction functions: curve *C* is an ocean-no-ocean function, curve *D* is a coastline function, and curve *E* is an earthquake activity function.

The ocean-no-ocean function in curve *C* equals 1 for directions from LASA to open oceans and 0 in the directions to the Arctic ocean, Bering Sea, and Gulf of Mexico. We exclude the Gulf of Mexico as a region not likely to contain strong low-frequency ocean swell. The one example (sample set S20) showing strong seismic noise from hurricane Beulah was excluded from the time-averaged results as being atypical.

The coastline function (curve *D*) is proportional to the length of coast

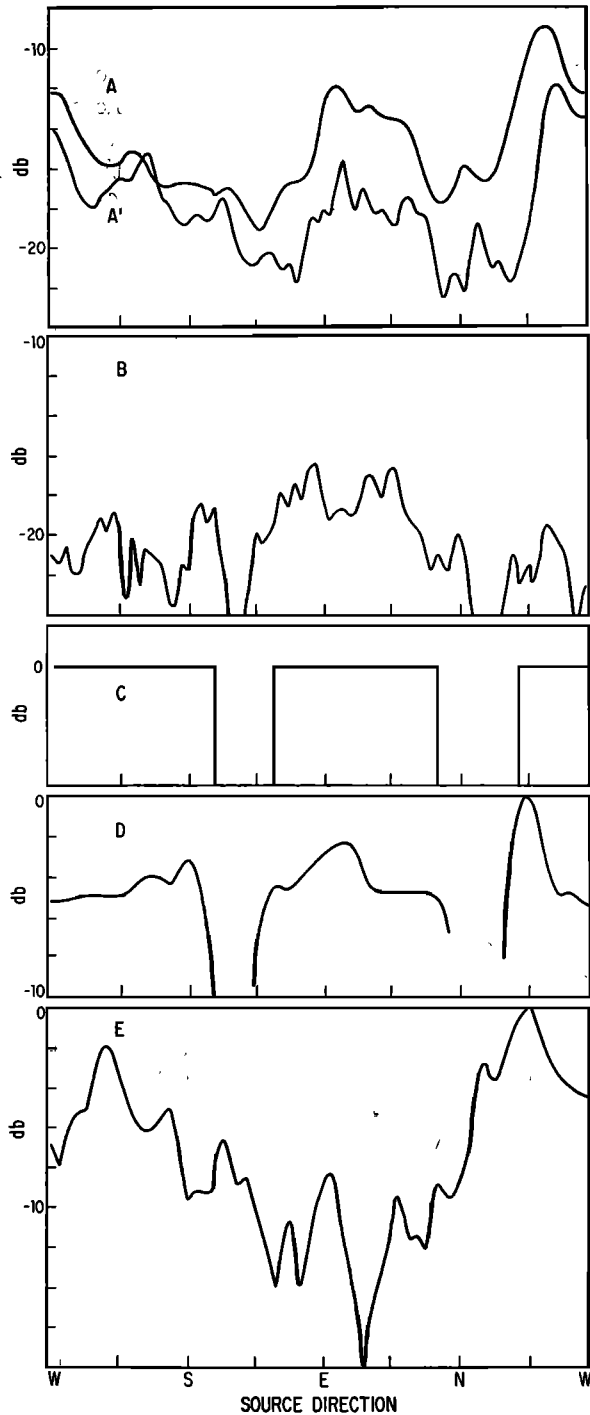


Fig. 28. Time-averaged directional spectra of *A*, PF vertical Rayleigh motion, 60–90 mHz; *A'*, DF vertical Rayleigh motion, 120–155 mHz; *B*, higher mode vertical Rayleigh motion, 160–195 mHz; *C*, ocean–no-ocean function; *D*, coastline function; and *E*, earthquake activity function.

divided by its distance in each direction. This function represents the expected directional spectrum for a model in which equal lengths of coast generate equal amounts of seismic noise power and the seismic power diminishes with distance owing to geometrical spreading.

The earthquake function (curve *E*) estimates the relative seismic power arriving at LASA from worldwide shallow earthquakes as a function of direction. From a set of 3300 shallow events above magnitude 5 (taken from the U. S. Coast and Geodetic Survey Earthquake Data Reports), each event was weighted by 1 divided by its distance from LASA. Curve *E* is this weighted count per unit angle as a function of direction to the sources.

All three of the average directional spectra resemble the ocean-no-ocean function to the extent that the seismic noise power is lowest in the no-ocean directions. The average PF and DF directional curves are remarkably similar. They resemble more the coastline function than the ocean-no-ocean function. The major discrepancy between PF and DF and function in curve *D* is the lower seismic power between east and southeast and between south and southwest. This may indicate that the average ocean-wave power is lower near coasts along the southern part of North America.

The directional spectrum for DF tends to differ from that of PF more on an individual day than it does on the average. If DF is predominantly generated near coastlines, we would expect similarity in the directional power of PF and DF for both daily and average observations, since both are generated by the same waves. However, we might expect that the angle of incidence of the ocean waves near a coast affects DF generation more than PF generation. This effect would produce daily differences between PF and DF directional spectra that would tend to decrease with long time averaging.

The average higher mode source directions are almost isotropic; they differ most from the PF and DF fundamental mode directions by lacking power from the west and northwest. We have found that for individual days the higher modes show peak power from the direction of storms off the Atlantic and Gulf of Mexico coasts. From this observation we are led to conclude that higher modes are associated with ocean waves. On the other hand, the results from single-day records show the same absence of peak power from the north to southwest as the time average results.

The three types of surface wave seismic noise all show evidence of sources near ocean coastlines. We find no evidence that significant DF in the band 120–155 mHz comes from sources other than those near coasts. The earthquake activity function differs considerably from the coastline functions. All three seismic noise types show directional distribution different from that expected from earthquakes.

7. CONCLUSIONS

1. PF surface wave noise generation in the frequency band 60–90 mHz can be explained by ocean waves near coasts. Directional spectra at LASA are consistent with the hypothesis that most of the energy comes from coastlines in the vicinity of large storms, but all coastal areas appear to contribute.

2. DF surface waves in the frequency band 120–160 mHz come mostly from coastline areas. No evidence in our results indicates pelagic sources near storms; this contrasts with the situation for higher-frequency body waves that come from the wake of storms. Seven-sec microseisms are usually poor storm trackers, explaining some of the difficulties in attempts to use them for this purpose [Gilmore, 1946]. Iyer [1958] found some microseisms originating from the direction of storms far at sea. The examples were for two storms that moved across the North Atlantic at speeds up to 20° /day, a speed well above the group velocity of most ocean waves. We conclude that coastal reflection of ocean waves is responsible for most DF seismic generation, except at frequencies well above the critical frequency when a storm moves faster than its waves. Only storms moving considerably faster than 10° /day generate 7-sec microseisms at sea in the vicinity of the storm.

3. Body waves tend to dominate seismic noise above about 200 mHz. The results indicate generation by the same mechanism as DF surface waves. Source areas include those near coastlines that are due to ocean wave reflection as well as regions in the wake of storms. The regions in storm wakes are generators for storms moving sufficiently fast.

4. There is no evidence that seismic noise is related to earthquakes. Our earthquake activity function was found for large events; we expect that the more numerous small events have a similar geographic distribution. We studied only sample sets that were free of obvious earthquakes; the background seismic level due to the many small earthquakes is below that of the seismic noise from oceans.

5. The vertical seismic ground motion is dominated by fundamental Rayleigh mode below 160 mHz. Above that frequency, higher modes tend to predominate. At least two higher modes have been recognized in the LASA data. Horizontal motion consists of both Love and Rayleigh modes below 200 mHz; the horizontal power is roughly equal in each, but there are indications that the Love-to-Rayleigh power ratio may be frequency dependent.

6. At any given time, Love waves are likely to come from the same directions as Rayleigh waves, suggesting that Love wave noise originates near coastlines.

7. Higher mode Rayleigh waves come from well-defined directions corresponding to storm directions to the east or south. We have no explanation for the conspicuous lack of power from directions between northwest and southwest.

Acknowledgments. Dr. Richard Haubrich was supported under Air Force contract AF49(638)-1388 with the University of California, San Diego, and Dr. Keith McCamy was supported under Air Force contract AF19(628)-4082 between the Air Force Cambridge Research Laboratories and Lamont-Doherty Geological Observatory, Columbia University, as part of the Vela Uniform Program sponsored by the Advanced Research Projects Agency of the Defense Department. The Institute for Space Studies, Columbia University, generously provided computing facilities for some of this work.

REFERENCES

- Abramovici, F., Diagnostic diagrams and transfer functions for oceanic wave guides, *Bull. Seismol. Soc. Am.*, 58, 427–456, 1968.

- Darbyshire, J., Structure of microseismic waves: Estimation of direction of approach by comparison of vertical and horizontal components, *Proc. Roy. Soc. London, A*, **223**, 96-111, 1954.
- Darbyshire, J., Microseisms, in *The Sea*, vol. 1, pp. 700-719, John Wiley, London, 1962.
- Darbyshire, J., A study of microseisms in South Africa, *Geophys. J.*, **8**, 165-175, 1963.
- Forbes, C. B., R. Oberchain, and R. J. Swain, The LASA sensing system design, installation, and operation, *Proc. IEEE*, **53**, 1834-1843, 1965.
- Gilmore, M. H., Microseisms and ocean storms, *Bull. Seismol. Soc. Am.*, **36**, 89-119, 1946.
- Gutenberg, B., Microseisms, in *Advances in Geophysics*, **5**, pp. 53-92, Academic, New York, 1958.
- Gutenberg, B., and F. Andrews, *Bibliography of Microseisms*, 2nd ed., 134 pp., Seismological Laboratory, California Institute of Technology, Pasadena, 1956.
- Hasselmann, K., A statistical analysis of the generation of microseisms, *Rev. Geophys.*, **1**, 177-209, 1963.
- Haubrich, R. A., Microseisms, in *International Dictionary of Geophysics*, edited by S. K. Runcorn, Pergamon, London, 1967.
- Haubrich, R. A., Array design, *Bull. Seismol. Soc. Am.*, **58**, 979-991, 1968.
- Haubrich, R. A., W. H. Munk, and F. E. Snodgrass, Comparative spectra on microseisms and swell, *Bull. Seismol. Soc. Am.*, **53**, 27-37, 1963.
- Hjortenber, E., *Bibliography of Microseisms, 1955-1964*. Geodaetisk Instituts Skrifter **3**, Raekke Bind 38, Bianco Lunos Bogtrykkeri A/S, Copenhagen, 1967.
- Iyer, H. M., A study of direction of arrival of microseisms at Kew Observatory, *Geophys. J.*, **1**, 32-43, 1958.
- Iyer, H. M., Composition and propagation of storm microseisms, Ph.D. thesis, University of London, 1959.
- Iyer, H. M., History and science of microseisms, *VESIAC state art rept. 4410-64-x*, 1964.
- Longuet-Higgins, M. S., A theory of the origin of microseisms, *Phil. Trans. Roy. Soc. London, A*, **243**, 1-35, 1950.
- Longuet-Higgins, M. S., Can sea waves cause microseisms? in *Symposium on Microseisms, U. S. Natl. Acad. Sci. Publ. 306*, 74-93, 1952.
- Oliver, J., A world-wide storm of microseisms with periods of about 27 seconds, *Bull. Seismol. Soc. Am.*, **52**, 507-517, 1962.
- Oliver, J., and R. Page, Concurrent storms of long and ultralong period microseisms, *Bull. Seismol. Soc. Am.*, **53**, 15-26, 1963.
- Toksöz, M. N., and R. T. LaCoss, Microseisms: Mode structure and sources, *Science*, **159**, 872-873, 1968.
- Wiechert, E., Verhandlugen der zweiten Internationalen Seismologischen Konferenz, *Gerlands Beitr. Geophys.*, **2**, 41-43, 1904.

(Manuscript received October 29, 1968.)